

Cyclic Voltammetric Study of Intramolecular and Intermolecular Hypervalent Organoantimony Complexes with Sb···N Bonding

Katsuyoshi Hoshino,^{*,†} Tomohisa Ogawa,[†] Shuji Yasuike,^{*,§} Hiroko Seki,[‡] Jyoji Kurita,[§] Tatsuhiro Tokunaga,[‡] and Kentaro Yamaguchi[‡]

Faculty of Engineering and Chemical Analysis Center, Chiba University, Inage-ku, 1-33 Yayoi-cho, Chiba 263-8522, Japan, and Faculty of Pharmaceutical Sciences, Hokuriku University, Ho-3 Kanagawa-Machi, Kanazawa 920-1181, Japan

Received: August 27, 2004

The electrochemical behaviors of a series of four intramolecular hypervalent complexes containing Sb···N bonding (antimony (III, V) compounds) and of the relevant common precursors, organonitrogen and (tri- and penta-) substituted stibines, have been investigated using cyclic voltammetry. The shape of the voltammograms is not the simple superposition of the precursors, and the antimony centers of all the complexes undergo an irreversible oxidation process consisting of a charge transfer preceded by the first-order formation–dissociation equilibrium of the complexes. The detailed analysis of the oxidation current, when combined with the theoretical treatment by Nicholson and Shain, provides information on the status of the Sb···N bonding. Good correlations between the electrochemical parameters derived from the oxidation current and the Sb···N bond distance are obtained. Additionally, the cyclic voltammetry of a mixture of the precursors leads to the discovery of their intermolecular hypervalent complexes.

1. Introduction

Hypervalent compounds have long attracted both experimental and theoretical attention because of their intriguing chemical and biological activities.^{1–18} Recently, we prepared various triaryl antimony(III, V) compounds bearing phenyl and naphthyl substituents with $-\text{CH}_2\text{NMe}_2$ in the ortho position and revealed the hypervalent Sb···N bonding structures by means of ^1H – ^{13}C and ^1H – ^{15}N heteronuclear multiple bond correlation (HMBC) experiments,¹⁹ X-ray crystallography, and semi-empirical theoretical calculations.^{20–22} We have also demonstrated a remarkable reactivity enhancement by the Sb···N transannular hypervalent coordination of ethynyl-1,5-azastibocines in the palladium-catalyzed cross-coupling reaction with organic halides.²³ These findings prompted us to study the electrochemical behaviors of the triarylstibines with the intramolecular Sb···N interactions, because these interactions should perturb the electronic character of the redox-active Sb···N moiety and, therefore, the electrochemical properties such as the redox potentials, electrode kinetics, reaction pathways, and so forth. Studies of the electrochemical redox reactions of trisubstituted stibines have been rarely studied, and to a smaller extent, the electrode reactions of hypervalent organoantimony compounds,^{24–26} though compounds containing antimony have attracted great attention over the past decade because of their application as heterogeneous catalysts^{27–29} and precursors for superconducting materials in metal organic chemical vapor deposition (MOCVD) processes.^{30,31}

In this study, detailed cyclic voltammetric (CV) measurements^{32–34} were conducted for four hypervalent stibines with the Sb···N bonding as well as their constituent (tri- and penta-)

substituted stibines and organonitrogen compounds, and their specific redox behaviors are interpreted in terms of their previously reported physicochemical properties. More important, we extended the measurements to the three mixed systems of organonitrogen and stibines, leading to the discovery of the corresponding intermolecular hypervalent complexes. To the best of our knowledge, no intermolecular types of complexes containing antimony as the central atom have been previously prepared and characterized.

2. Experimental Section

2.1. Materials. The intramolecular hypervalent compounds **4**, **6**, **7**, and **8** (see Chart 1) were synthesized according to previously reported procedures.^{20,21} Compounds **2** and **3** were prepared according to refs 35 and 36, respectively. The triphenylstibine **5** (99%) and benzyldimethylamine **1** (98%) were purchased from Aldrich. The acetonitrile solvent was from Kanto Chemicals, Ltd., (spectroscopic grade, >99.7%) and used without further purification: the water content was 0.03 wt %, corresponding to 22 mM. The addition of 20 vol % CH_2Cl_2 (spectroscopic grade, >99.8%, Kanto Chemicals, Ltd.) to CH_3CN was required to dissolve 1.0 mM of **8**. Tetrabutylammonium perchlorate (TBAP, Tokyo Kasei Kogyo Co., Ltd., >98%) as a supporting electrolyte was also used as supplied.

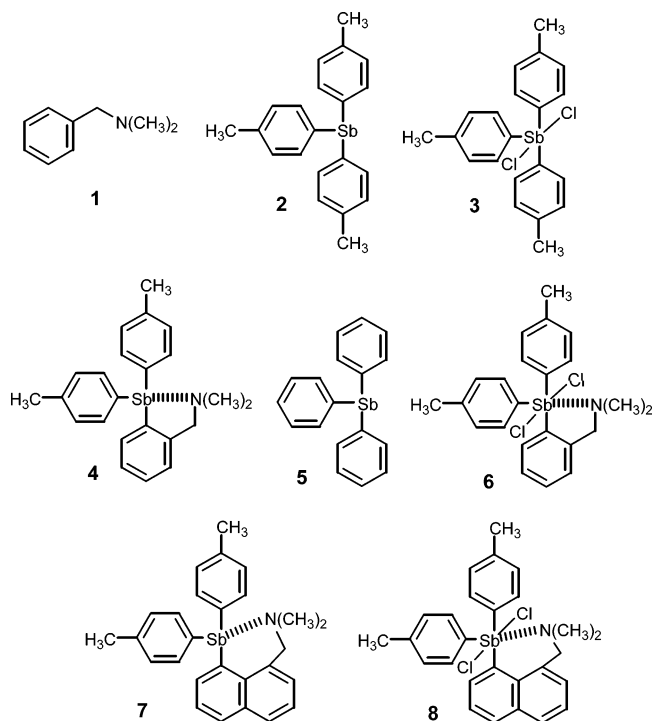
2.2. Cyclic Voltammetry. All CV experiments were performed using a Hokuto-Denko Model HAB-151 potentiogalvanostat connected to a Riken-Denshi model F-35C recorder. A three-electrode cell assembled with a Pt disk working electrode (BAS Co., Ltd.; geometric area = 0.021 cm^2), a Pt plate counter electrode (2 cm^2), and a saturated calomel reference electrode (SCE; TOA Co.) was used. Prior to each experiment, the working Pt electrode was polished on a felt disk (Buehler) using aqueous slurries of diamond (BAS Co., Ltd.; grain size = 1 μm) and alumina (BAS Co., Ltd.; grain size = 0.05 μm), rinsed in distilled–deionized water, and then

* To whom correspondence may be addressed. E-mail: k_hoshino@faculty.chiba-u.jp (K.H.); s-yasuike@hokuriku-u.ac.jp (S.Y.).

[†] Faculty of Engineering, Chiba University.

[‡] Chemical Analysis Center, Chiba University.

[§] Faculty of Pharmaceutical Sciences, Hokuriku University.

CHART 1: Hypervalent Complexes (4, 6, 7, and 8) and the Relevant Common Precursors (1, 2, and 3)^a


^a The analogous stibine (5) was also employed in the electrochemical investigations.

subjected to ultrasonic cleaning in water, acetone, and tetrahydrofuran (each 10 min). The voltammetric measurements were carried out in solutions deaerated by bubbling with 99.9% pure nitrogen, and the same gas was passed over the solution during the experiments at room temperature. Simulations of the cyclic voltammograms were performed using the simulation software attached to the ALS Model 750A.

3. Results and Discussion

3.1. Voltammetric Behavior of Precursors 1, 2, and 3.

Curves a and b in Figure 1 show the cyclic voltammograms of 1 and 2 in CH₃CN at a sweep rate (ν) of 50 mV s⁻¹.³⁷ They

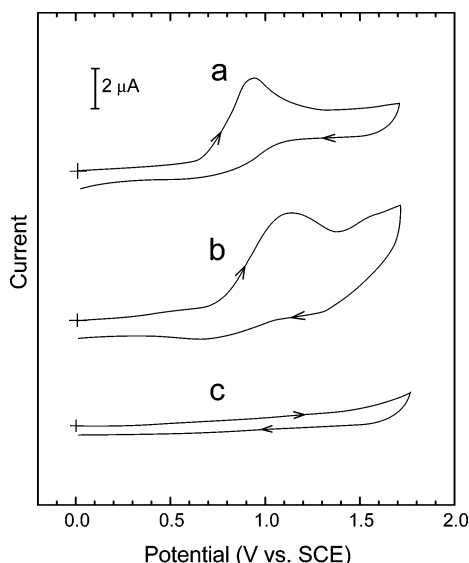


Figure 1. Cyclic voltammograms of 1.0 mM of 1 (a), 2 (b), and 3 (c) in CH₃CN containing 0.1 M of TBAP: sweep rate, 50 mV s⁻¹; working electrode, Pt disk (0.021 cm²).

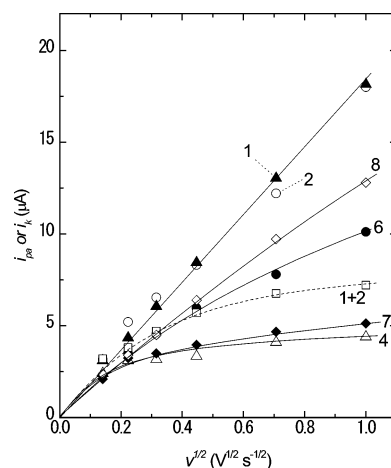
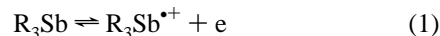


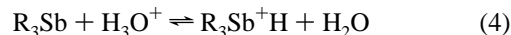
Figure 2. Dependence of i_{pa} (or i_k) on $\nu^{1/2}$ for the compounds 1 (\blacktriangle), 2 (\circ), 4 (\triangle), 6 (\bullet), 7 (\blacklozenge), 8 (\diamond), and a mixture of 1 and 2 (\square).

were oxidized in electrochemically irreversible processes followed by chemical reactions.^{24,37} As expected from the higher electron donating ability of N compared to Sb,³⁸ 2 was oxidized at slightly higher potentials (oxidation peak potential = 1.12 V vs SCE) compared to 1 (0.92 V vs SCE). The dependence of the peak current, i_{pa} , on $\nu^{1/2}$ for compounds 1 and 2 gave straight lines intersecting at the origin (see Figure 2: \blacktriangle , 1; \circ , 2), indicating that their oxidations are diffusion-controlled³² in the range of $\nu = 20$ –1000 mV s⁻¹: The characteristic lifetime of the coupled chemical reactions can be regarded as small compared to the experimental duration of the electrochemical attack. The voltammogram of 3 (curve c) showed no waves in the potential range employed and was equal to the background current measured in a CH₃CN solution containing 0.1 M of TBAP; the introduction of two electronegative chlorine atoms into 2 results in a positive shift of the oxidation wave of the antimony center beyond the potential window.

Nikitin et al.^{24,37} measured the voltammograms of 2 and 5, and proposed their electrooxidation mechanism corresponding to the irreversible wave of 2 at 1.12 V in Figure 1



where R indicates an aryl or alkyl group. In addition to the product-forming reactions (eqs 1–3), a relatively slow reaction (eq 4) occurs which deactivates R_3Sb via protonation by the protons liberated in reaction 2



This reaction affects the number of electrons involved in reactions 1–3, n ; $n = 1.43$ and 1.47 were experimentally found for 2 and 5, respectively.³⁷ On the time scale of the preparative electrolysis, $R_3Sb^{+}OH$ ($R = \text{phenyl}$) dimerizes and eliminates water to yield $[R_3SbOSbR_3]^{2+}$.³⁹ On the basis of these studies, a quasireversible wave, observed in the voltammogram of 2 at ca. 1.5 V, would likely be assigned to the oxidation of $[R_3SbOSbR_3]^{2+}$, $R_3Sb^{+}OH$, or $R_3Sb^{+}H$. As a good approximation, the overall reaction for the electrooxidation of R_3Sb (eqs 1–4) may be described as a totally irreversible charge transfer



We should note again that the apparent value of n for eq 5 differs from $n = 2$ ($n = 1.43$ and 1.47 for **2** and **5**, respectively), because R_3Sb is partially deactivated at the first oxidation potential as described already (eq 4). The validity of this approximation will be tested later and help to extract kinetic information for the electrochemistry of **4**, **6**, **7**, and **8**.

3.2. Trisubstituted Stibine (4**) with Intramolecular Hypervalent Bonding.** Curve a in Figure 3 shows the cyclic voltammogram for the oxidation of **4** in CH_3CN at $\nu = 50$ mV s^{-1} . The shape of the voltammogram was not the simple superposition of curves a and b in Figure 1, and a new irreversible oxidation wave appeared at the potential of $+0.46$ V, lower than those of **1** and **2**. In our previous study,²⁰ electron donation from the nitrogen moiety to the antimony moiety⁴⁰ formed the hypervalent bonding, $Sb^{\delta-} \cdots N^{\delta+}$, within the molecules of **4** and **6**. This allows us to assign the wave at $+0.46$ V to the oxidation of the $Sb^{\delta-}$ moiety in **4**. The quasireversible wave at ca. 1.5 V may be attributed to the oxidation of the reaction product formed at $+0.46$ V from an analogy with voltammogram b in Figure 1. When we concentrate on the oxidation at $+0.46$ V, the electrode reaction is expected to be the case in which a first-order chemical reaction precedes an irreversible charge transfer (eqs 6 and 7)



where 4_B and 4_N denote the molecular structures of **4** with and without intramolecular hypervalent bonding, respectively, and k_f and k_b are the forward and backward rate constants for the chemical reaction, respectively.

According to the theory of Nicholson and Shain,³⁴ the kinetic current, i_k , shows the following dependence on ν for the irreversible charge transfer preceded by a first-order chemical reaction

$$i_d/i_k = 1.02 + \frac{0.531\sqrt{b}}{K\sqrt{l}} \quad (8)$$

$$\text{with } b = \frac{\alpha n_a F \nu}{RT}, l = k_f + k_b, \text{ and } K = k_f/k_b \quad (9)$$

where i_d is the diffusion-controlled current that flows when the preceding reaction has no effect on the charge-transfer reaction, α is the transfer coefficient, and n_a is the number of electrons involved in the rate-determining step, and the other symbols (R , T , and F) denote their usual meanings. If we assume that the oxidation peak current for **2** (indicated in Figure 1) can be taken as i_d and substitute the measured current at $+0.46$ V ($i_k(\mathbf{4})$) for i_k , the left-hand side of eq 8 can be calculated. The choice of the i_d current is reasonable in that (1) the microenvironment of antimony in the molecule of **2** corresponds to that in **4** without the interaction with the nitrogen moiety, and (2) the oxidation current for **2** is diffusion-controlled as was evidenced by the $i_{pa}-\nu^{1/2}$ plot (open circles in Figure 2). These are the requisites for the use of eqs 8 and 9. Curve a in Figure 4 shows the plot of $i_d/i_k(\mathbf{4})$ versus $\nu^{1/2}$. The linear relationship intersecting the i_d/i_k axis at ca. 1 supports the expected reaction mechanism indicated by eqs 6 and 7, which involves the irreversible charge transfer preceded by a reversible first-order chemical reaction.

The forward (k_f) and backward (k_b) rate constants in eq 6 can be obtained from the slope of curve a in Figure 4. On the basis of eqs 8 and 9, the slope is described as $3.34(\alpha n_a)^{1/2} k_f^{-1} k_b$ (k_f

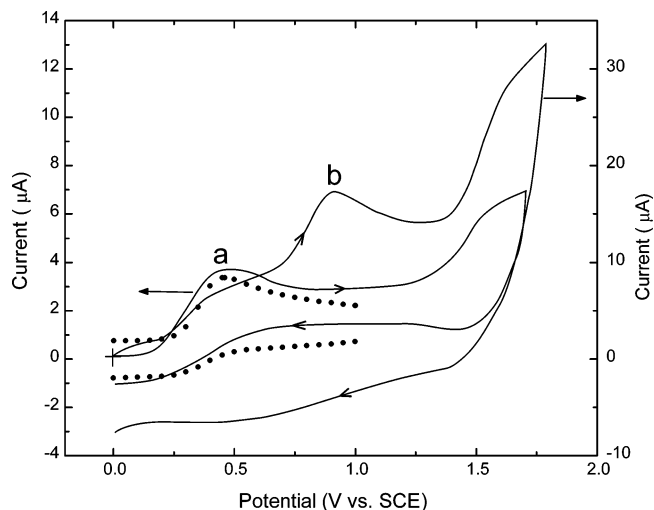


Figure 3. Cyclic voltammograms of **4** (1.1 mM) in $CH_3CN/TBAP$ (0.1 M) at $\nu = 50$ (a) and 1000 mV s^{-1} (b). The closed circles represent the simulated result (for details, see text).

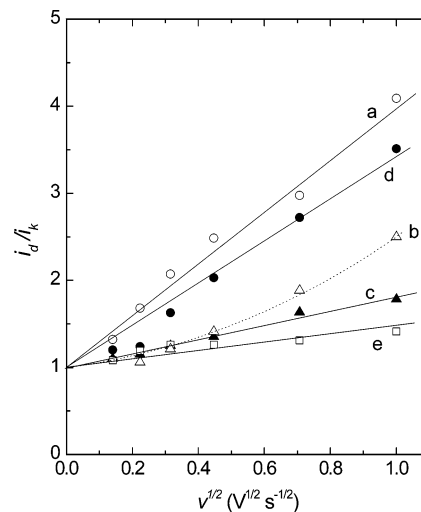


Figure 4. Plots of i_d/i_k versus $\nu^{1/2}$ for the compounds **4** (a), **6** (c), **7** (d), **8** (e), and the mixture of **1** and **2** (b).

$+ k_b)^{-1/2}$, and thus, the values of k_f and k_b can be simulated by knowing the product αn_a . The value of αn_a was derived from the slope of the $i_{pa}-\nu^{1/2}$ plot for **2** (open circles in Figure 2) under the assumption that αn_a is the same for all the antimony compounds employed. The irreversible charge transfer of **2**, $2 \rightarrow 2^+ - OH$, follows the relationship:^{32,33}

$$i_p = (2.99 \times 10^5) n(\alpha n_a)^{1/2} A C_R^* D_R^{1/2} \nu^{1/2} \quad (10)$$

where A , C_R^* , and D_R denote the area of the working electrode (0.021 cm²), the concentration of **2** in the solution (1.0 mM), and the diffusion coefficient of **2**, respectively. Substitution of a typical value of D_R , 10^{-5} cm²/s, into eq 10 allowed us to calculate the value of αn_a , 0.45 , and, in turn, simulate the values of k_f and k_b by constructing a simple program. The rate constants thus determined are summarized in Table 1 as well as the equilibrium constant, $K (= k_f/k_b)$.

The validity of these rate constant values was tested by a digital simulation^{41,42} of the cyclic voltammogram for **4**. The points in Figure 3 represent the simulated current–potential curve for the wave at 0.46 V (indicated by eqs 6 and 7). The simulation parameters are $k_f = 0.83$ s⁻¹, $k_b = 3.1$ s⁻¹ (see Table 1), $E^\circ(\mathbf{4}) = 0.16$ V, $k^\circ(\mathbf{4}) = 1.0 \times 10^{-4}$ cm s⁻¹, $D = 1.0 \times$

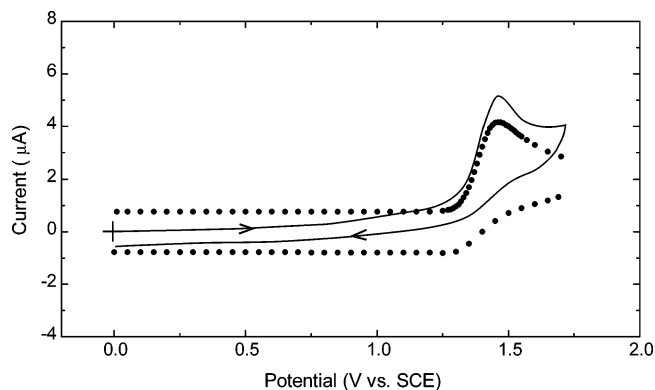
TABLE 1: Electrokinetic Parameters for the Oxidation of 4, 6, 7, and 8

compound	k_f (s ⁻¹)	k_b (s ⁻¹)	K	$S(V^{-1/2} s^{1/2})$
4	0.83	3.1	0.27	3.0
6	0.87	1.0	0.87	0.82
7	0.52	1.1	0.47	2.4
8	0.48	0.30	1.6	0.48

$10^{-5} \text{ cm}^2 \text{ s}^{-1}$, $n = 1.47$, $\alpha = 0.5$, and $C_d = 15 \mu\text{F}$ where $E^\circ(4)$ and $k^\circ(4)$ are the standard potential and the heterogeneous rate constant for the electrooxidation of **4**_B (eq 7), respectively, D denotes the diffusion coefficient of the species involved in the electrode reactions which is again assumed to be the same as the typical value, and C_d is the double-layer capacitance. The experimental wave at 0.46 V was reproduced by the digital simulation, indicating that the values taken for k_f and k_b are reasonable and being additional evidence for the CE (electron transfer preceded by a chemical reaction) mechanism for the electrooxidation of **4**.

Additional information on the complex formation–dissociation equilibrium was also obtained from the voltammograms measured by varying sweep rates. With increasing ν , the wave at +0.46 V became indistinct and made little contribution to the electrode reaction above $\nu \approx 1000 \text{ mV s}^{-1}$ (see the curve b in Figure 3). The plot of $i_k(4)$ at +0.46 V versus $\nu^{1/2}$ (open triangles in Figure 2) deviated from a straight line, and the deviation increased with increasing ν . This means that the departure from equilibrium of the chemical reaction, which is created by the consumption of **4**_B at the electrode surface, is not compensated because of the small rate constants, k_f 's. Support for the mechanistic feature was found in the dependence of the voltammogram shape on ν . As is demonstrated in Figure 3b, the growth of the wave at 0.9 V with ν was observed and may be ascribed to the superposition of the oxidation waves of the antimony and nitrogen moieties in **4**_N. The observation of the separate waves implies that the rate of the formation–dissociation of **4** is slow compared to the experimental duration of the electrode reaction.⁴³

3.3. Pentasubstituted Stibine (6) with Intramolecular Hypervalent Bonding. Figure 5 shows the cyclic voltammogram of **6** in CH₃CN at $\nu = 50 \text{ mV s}^{-1}$. In contrast to the voltammograms in Figures 3a (for **4**), an irreversible single wave with a peak current of $i_k(6)$ was observed at 1.46 V, and its shape showed no dependence on ν . The plot of $i_d/i_k(6)$ versus $\nu^{1/2}$ gave a straight line with the intercept of ca. 1 on the $i_d/i_k(6)$ axis (curve c in Figure 4), indicating that the wave is attributed to the oxidation of the antimony moiety in **6** and the oxidation obeys a reaction mechanism similar to that for the oxidation of **4** (eqs 6 and 7). The positive shift in the oxidation wave relative to **4**, 0.46 V, can be explained by the attachment of electronegative chlorine atoms to the antimony; the absence of the oxidation wave for the oxidation product at 1.46 V is probably due to its positive shift beyond the potential window. Notable is the large difference in the slopes of the plots in Figure 4 between **4** (slope of the curve a = $3.1 \text{ V}^{-1/2} \text{ s}^{1/2}$) and **6** (slope of the curve c = $0.8 \text{ V}^{-1/2} \text{ s}^{1/2}$). According to eqs 8 and 9, the slope is proportional to $\{\alpha n_d/k_f K(K+1)\}^{1/2}$. If we assume that the product of αn_d is only slightly affected by the introduction of Cl, the difference is based on the enhancement of the values of K and/or k_f . The effect of the enhancement is also reflected in the plot of $i_k(6)$ versus $\nu^{1/2}$ (closed circles in Figure 2). The relationship of $i_k(6) > i_k(4)$ in the figure would be an indication that the increase in K and/or k_f favors access of a larger amount of the hypervalent structure to the electrode surface. In our previous study,²¹ the X-ray diffraction (XRD) and NMR

**Figure 5.** Cyclic voltammogram of **6** (1.0 mM) in CH₃CN/TBAP (0.1 M) at $\nu = 50 \text{ mV s}^{-1}$. Closed circles: Simulation using parameters given in the text.

analyses of **4** and **6** were conducted and revealed that the antimony (V) compound (**6**) involves a stronger interaction of the $\text{Sb}^{\delta-} \cdots \text{N}^{\delta+}$ bond compared to the antimony (III) compound (**4**), which was explained by the promotion of the valence extension because of an increased Lewis acidity on the antimony caused by the introduction of two Cl atoms. These results allow us to assume that the slope of the plots in Figure 4 is determined by K and the slope is a good indication of the extent of the $\text{Sb}^{\delta-} \cdots \text{N}^{\delta+}$ interaction: the more intimate the interaction, the lower the slope. This assumption was supported by comparing the simulated K and k_f values of **6** with those of **4** in Table 1. The K value of **6** is greater than that of **4**, but with their values of k_f nearly the same.

The points in Figure 5 show the voltammogram for **6** reproduced by the digital simulation where $k_f = 0.87 \text{ s}^{-1}$, $k_b = 1.0 \text{ s}^{-1}$ (see Table 1), $E^\circ(6) = 1.36 \text{ V}$, and $k^\circ(4) = $2.5 \times 10^{-3} \text{ cm}^2 \text{ s}^{-1}$, while the other parameters have the same values as in Figure 3. The difference in the current between the experimental and simulated voltammograms is due to the approximations of the double-layer capacitance (C_d) used in the program. The program assumes that the value of C_d is constant over the entire potential range, but the experimental value of C_d increased with the increasing potential, as was demonstrated by the background current. The simulated peak current at 1.46 V approached the experimental one when corrected for the difference in C_d between the simulated (15 μF) and the experimental (30 μF at 1.46 V) voltammograms.$

3.4. Stibines (7 and 8) Designed to Enhance the Hypervalent Interactions. The cyclic voltammograms of **7** measured at 50 (curve a in Figure 6) and 1000 mV s^{-1} (curve b) are quite similar in shape and sweep-rate dependence to those of **4** (Figure 3). Indeed, the plot of $i_d/i_k(7)$ versus $\nu^{1/2}$ gave a straight line intersecting the y-axis at ca. 1 (the curve d in Figure 4) where $i_k(7)$ is the current at 0.54 V. This demonstrates that the charge transfer at 0.54 V can be assigned to the oxidation of the $\text{Sb}^{\delta-}$ moiety in **7**_B ($7_B \rightarrow 7_B^+ - \text{OH}$) and is preceded by the formation of the hypervalent complex ($7_N \rightleftharpoons 7_B$). More important, the slope of the plot is lower than that of **4**, curve a in Figure 4. On the basis of the rationale described in sections 3.2 and 3.3, the result suggests that the $\text{Sb}^{\delta-} \cdots \text{N}^{\delta+}$ interaction in **7**_B is more intimate than that in **4**_B, being supported by the results in Figure 2 (◆) (i.e., $i_k(7) > i_k(4)$) and the higher simulated value of K for **7** compared with that for **4** (see Table 1). This increase in the interaction presumably reflects the more flexible conformation of **7** relative to **4** that allows the nitrogen atom to more closely approach the antimony.²¹

The digital simulation of curve a in Figure 6 produced points in the same figure if we take the values of $k_f = 0.52 \text{ s}^{-1}$, $k_b =$

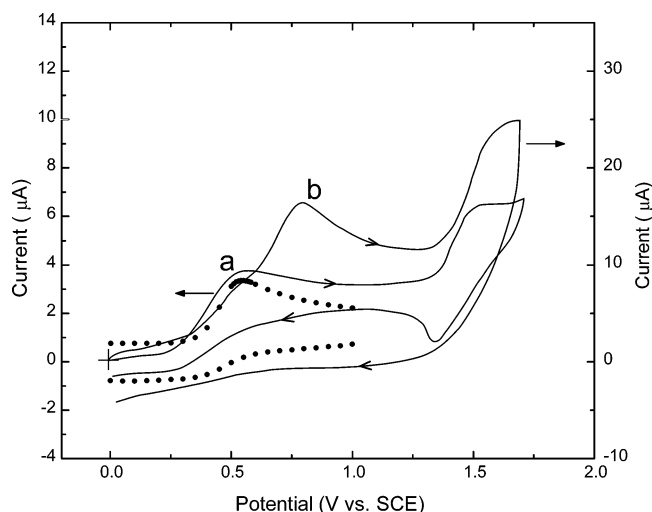


Figure 6. Cyclic voltammograms of **7** (1.0 mM) in $\text{CH}_3\text{CN}/\text{TBAP}$ (0.1 M) at $\nu = 50$ (a) and 1000 mV s^{-1} (b). The closed circles represent the simulated result (for details, see text).

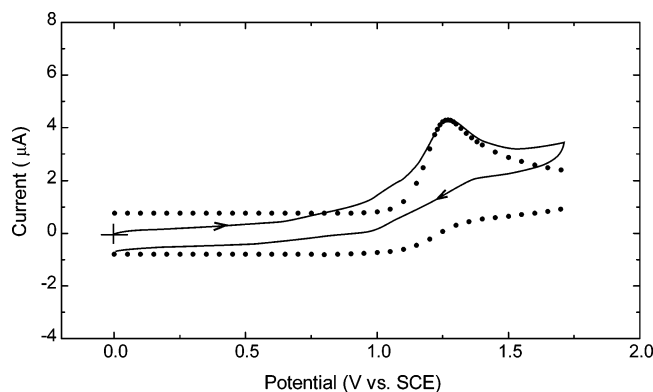


Figure 7. Cyclic voltammogram of **8** (1.0 mM) in a mixed solvent of CH_3CN and CH_2Cl_2 (4:1 vol ratio) containing 0.1 M of TBAP at $\nu = 50 \text{ mV s}^{-1}$. Closed circles: Simulation using parameters given in the text.

1.1 s^{-1} (see Table 1), $E^\circ(\mathbf{7}) = 0.27 \text{ V}$, and $k^\circ(\mathbf{7}) = 1.0 \times 10^{-4} \text{ cm s}^{-1}$ along with the other parameters being the same as those in Figures 3 and 5.

The electrochemical responses of **8** also show a striking resemblance to those of **6**. The voltammogram exhibited an irreversible wave (current = $i_k(\mathbf{8})$) at 1.27 V (Figure 7), a slightly lower potential than that of **6**, 1.46 V . The value of $i_d/i_k(\mathbf{8})$ again varies with $\nu^{1/2}$ in a linear fashion (the curve e in Figure 4), its slope, 0.4 , being lower compared to those for compounds **4**, **6**, and **7**. In addition, the deviation in the $i_k(\mathbf{8})-\nu^{1/2}$ plot (open diamonds in Figure 2) from the diffusion-controlled behavior is less pronounced than the plots for compounds **4**, **6**, and **7**. All of these results are consistent with the charge transfer of $\mathbf{8}_\text{B}$ ($\mathbf{8}_\text{B} \rightarrow \mathbf{8}_\text{B}^+ - \text{OH}$) preceded by the formation–dissociation equilibrium ($\mathbf{8}_\text{N} \rightleftharpoons \mathbf{8}_\text{B}$) that lies far to the right. This led us to conclude that the extent to which the antimony center interacts with the nitrogen moiety through hypervalent bonding in $\mathbf{8}_\text{B}$ is the largest among those of the employed hypervalent compounds, being supported by the largest K value obtained by the simulation for **8** (see Table 1). The cyclic voltammogram obtained by the digital simulation is shown as points in Figure 7 where $k_\text{f} = 0.48 \text{ s}^{-1}$, $k_\text{b} = 0.30 \text{ s}^{-1}$ (see Table 1), $E^\circ(\mathbf{8}) = 1.02 \text{ V}$, and $k^\circ(\mathbf{8}) = 1.0 \times 10^{-4} \text{ cm s}^{-1}$; the other parameters are the same as those in Figures 3, 5, and 6.

Table 2 summarizes the oxidation peak potential, E_ox , of the antimony center and the slope (S) of the $i_d/i_k-\nu^{1/2}$ plots for **4**,

TABLE 2: Electrochemical Parameters, Sb...N Bond Length, and ^{15}N -NMR Chemical Shift for **4, **6**, **7**, and **8****

compound	E_ox (V vs SCE)	S ($\text{V}^{-1/2} \text{ s}^{-1/2}$)	d (Å)	$^{15}\delta_\text{N}$ (ppm)
4	0.46^a	3.0	2.874	-350.7
6	1.46^a	0.82	2.584	-342.9
7	0.54^a	2.4	2.766	-349.3
8	1.27^a	0.48	2.59	-332.5
1 + 2 (mixture)	$\sim 0.6^b$			
1 + 3 (mixture)				
1 + 5 (mixture)				
1	0.92^c			-353.6
2	1.12^c			
3	d			
5	1.22^c			

^a Oxidation peak potential of the antimony center with intramolecular hypervalent bonding. ^b Oxidation peak potential of the antimony center with intermolecular hypervalent bonding. ^c Oxidation peak potential of the antimony center. ^d No oxidation waves in the potential range employed (~ 0 – 1.75 V vs. SCE). ^e Oxidation peak potential of the nitrogen center.

6, **7**, and **8**. Included in this table are the bond lengths of Sb...N, d 's, determined by XRD analysis and the ^{15}N chemical shift, $^{15}\delta_\text{N}$, obtained from the ^1H – ^{15}N HMBC experiment. These data were taken from our previous report.²¹ The values of d for **4**, **6**, **7**, and **8** are in the range between the sum of the van der Waals radii of 3.74 Å and the covalent bond length of 2.11 Å ; a low-field shift in the ^{15}N signal with decreasing d is caused by the electron deficiency around the nitrogen atom due to the delocalization of a pair of electrons, and is also the indication of the Sb...N interaction. Figure 8 shows the values of d (curves a and c) and $^{15}\delta_\text{N}$ (curves b and d) plotted versus S (top) and K (bottom). Although not a linear relationship except for curve c, good correlations were observed in these plots, indicating that CV and its related simulation are powerful tools for evaluating the status of the Sb...N bonding.

3.5. Trisubstituted Stibines (2, 3, and 5) with Intermolecular Hypervalent Bonding. The successful understanding of the redox systems described here is extended to the investigation of the intermolecular interaction between **1** and **2** (or **3**). Curve a in Figure 9 shows the cyclic voltammogram for the mixture of **1** and **2** in CH_3CN at $\nu = 50 \text{ mV s}^{-1}$. In this case, the shape of the voltammogram was also not a simple superposition of curves a and b in Figure 1, and a new irreversible oxidation wave appeared at a lower potential, ca. 0.6 V , than those of **1** and **2**. If we assume that an electron is donated from **1** to **2** to form the intermolecular hypervalent complex in which the antimony moiety in **2** is bonded to the nitrogen moiety in **1**, $\text{Sb}^{\delta-}(\mathbf{2})\cdots\text{N}^{\delta+}(\mathbf{1})$, the wave at ca. 0.6 V can be assigned to the oxidation of the $\text{Sb}^{\delta-}(\mathbf{2})$ moiety in the complex of **1**...**2**. Additionally, there were observed small signals at ca. 0.9 and 1.5 V , probably due to the oxidation of **1** and the second oxidation of **2**, respectively. The shape of the voltammogram was quite dependent on ν . The value of the current at ca. 0.6 V ($i_k(\mathbf{1} + \mathbf{2})$) quickly increased with ν below ca. 100 mV s^{-1} , but beyond this sweep rate, its increase was followed by a decrease in the increment (see curve b in Figure 9 recorded at 1000 mV s^{-1}), whereas the growth of the waves at ca. 0.9 , 1.1 , and 1.5 V with ν was observed which can be ascribed to the first oxidation of **1**, the first oxidation of **2**, and the second oxidation of **2**, respectively. The plot of $i_k(\mathbf{1} + \mathbf{2})$ versus $\nu^{1/2}$ (open squares in Figure 2) deviated from the diffusion-controlled behavior, and this deviation increased with increasing ν . Additionally, the value of $i_d/i_k(\mathbf{1} + \mathbf{2})$ showed no linear dependence on $\nu^{1/2}$ (curve b in Figure 4).

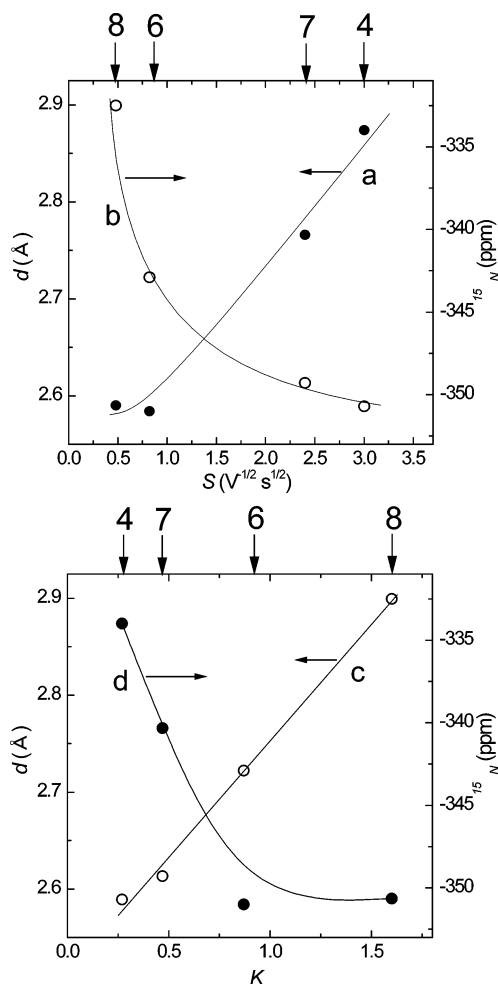


Figure 8. Correlations given by the $d - S$ (a), $^{15}\delta_N - S$ (b), $d - K$ (c), and $^{15}\delta_N - K$ plots (d). Top: The values of d and $^{15}\delta_N$ plotted vs S . Bottom: The values of d and $^{15}\delta_N$ plotted vs K .

All of these observations and interpretations thereof suggest that the electrode reaction of the mixture system could be based on the following mechanism involving the electrode reaction preceded by a second-order chemical step (eqs 11 and 12)



where k_f' and k_b' denote the forward (second order) and backward (first order) rate constants of the preceding chemical reaction, respectively. A theoretical treatment in such a case has been reported by Savéant and Xu,⁴⁴ in which it is assumed that the electrode reaction is reversible. However, this assumption is not the case for the present system and prevents us from using this treatment in the evaluation of the thermodynamic and kinetic parameters. Thus, the electrode behavior of the present system will hereafter be qualitatively treated. The deviation of the dotted curve in Figure 2 from a straight line means that the departure from equilibrium of eq 11, which is created by the consumption of $\mathbf{1} \cdots \mathbf{2}$ at the electrode surface, is not compensated because of the small rate constant of k_f' . This mechanistic feature is supported by the poorly characterized wave shape of curve b in Figure 9 due to the superposition of the waves for the oxidations of $\mathbf{1}$, $\mathbf{2}$, and $\mathbf{1} \cdots \mathbf{2}$. The observation of the separate waves, though not clearly defined because of the proximity of each wave, implies that the rate of the formation–dissociation

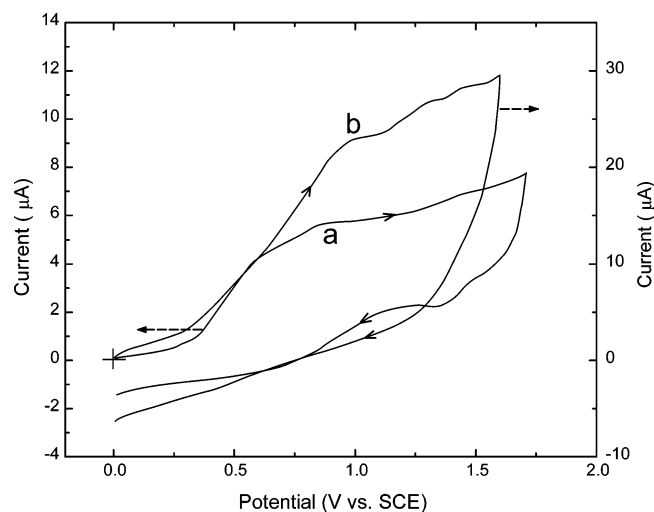


Figure 9. Cyclic voltammograms for the mixture of $\mathbf{1}$ (1.1 mM) and $\mathbf{2}$ (1.1 mM) in $\text{CH}_3\text{CN/TBAP}$ (0.1 M) at $\nu = 50$ (a) and 1000 mV s^{-1} (b).

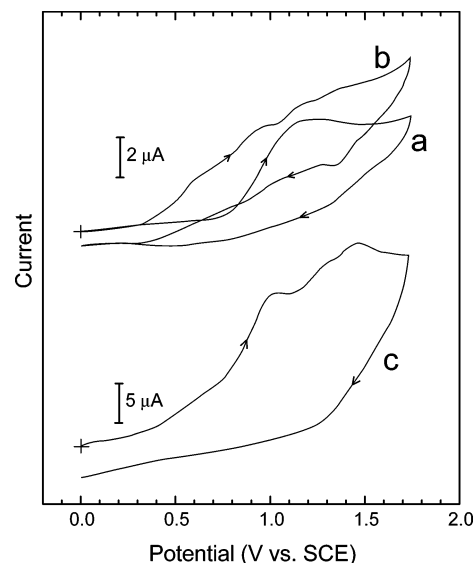


Figure 10. Cyclic voltammograms for $\mathbf{5}$ (1.0 mM) in $\text{CH}_3\text{CN/TBAP}$ (0.1 M) at $\nu = 50 \text{ mV s}^{-1}$ (a), and the mixture of $\mathbf{5}$ (1.0 mM) and $\mathbf{1}$ (1.0 mM) recorded at $\nu = 50$ (b) and 1000 mV s^{-1} (c).

of complex $\mathbf{1} \cdots \mathbf{2}$ is slow compared to the experimental duration of the electrode reaction.

This finding of the intermolecular hypervalent complex has prompted us to investigate the mixed systems of $\mathbf{1} + \mathbf{5}$ and $\mathbf{1} + \mathbf{3}$. Figure 10 shows the cyclic voltammograms for $\mathbf{5}$ (1 mM)³⁸ (a) and the mixture of $\mathbf{1}$ (1 mM) and $\mathbf{5}$ (1 mM) (b) in the TBAP (0.1 M)/ CH_3CN system at $\nu = 50 \text{ mV s}^{-1}$, and curve c is the voltammogram for the mixture recorded at 1000 mV s^{-1} . The appearance of a new wave at ca. 0.6 V, which is lower than the oxidation potentials of $\mathbf{1}$ and $\mathbf{5}$, and its sweep-rate dependence (not shown here) are similar to the electrochemical behaviors of $\mathbf{1} \cdots \mathbf{2}$ and, thus, would demonstrate the complex formation between $\mathbf{1}$ and $\mathbf{5}$.

A mixture of $\mathbf{1}$ and $\mathbf{3}$ gave a voltammogram (curve a in Figure 11, measured at 50 mV s^{-1}) showing their complexation more explicitly than the mixture of $\mathbf{1} + \mathbf{2}$ (curve a in Figure 9) and $\mathbf{1} + \mathbf{5}$ (curve b in Figure 10). On the basis of the considerations described already and the voltammograms of $\mathbf{1}$ and $\mathbf{3}$ (curves a and c in Figure 1, respectively), the first and the second oxidation waves (ca. 0.9 and 1.1 V, respectively) may well be attributed to the oxidations of $\mathbf{1}$ and the $\text{Sb}^{\text{d}}\text{-(3)}$ moiety in

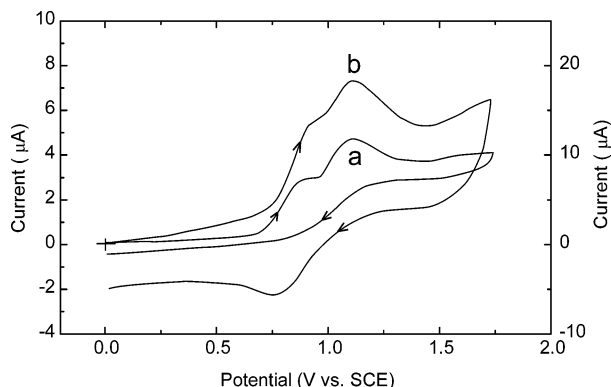


Figure 11. Cyclic voltammograms for the mixture of **1** (1.0 mM) and **3** (1.0 mM) in $\text{CH}_3\text{CN/TBAP}$ (0.1 M) at $v = 50$ (a) and 1000 mV s^{-1} (b).

complex **1**⋯**3** with the intermolecular hypervalent bonding of $\text{Sb}^{\delta-}(\text{3})\cdots\text{N}^{\delta+}(\text{1})$, respectively. The observation of the separate waves for **1** and **1**⋯**3** again implies the smaller rate constant for the formation of complex **1**⋯**3** compared to the experimental duration. The second oxidation current, $i_k(\text{1} + \text{3})$, cannot be investigated in a quantitative way because of the significant overlap with the second oxidation wave given by the first oxidation wave. However, in contrast to the oxidation wave of **1**⋯**2**, the wave of **1**⋯**3** is still clearly demonstrated at $v = 1000 \text{ mV s}^{-1}$ (curve b in Figure 8), suggesting that the complex formation–dissociation equilibrium (eq 11) lies more to the right in the mixed system of **1** and **3**.

4. Concluding Remarks

We have presented the first electrochemical evidence of the intra- and intermolecular hypervalent bonds formed between the antimony and nitrogen moieties by cyclic voltammetry and its simulations. The obtained results and mechanistic considerations present the feasibility of using an electrochemical technique in understanding the status of the hypervalent bondings, if the species involved in the linkage undergo electrode reactions and the time constant of the kinetic parameters is comparable to the time scale of the electrochemical experiment. We are beginning to extend these findings to include the analogous phosphines, arsines, and bismuthines, the results of which will be reported elsewhere.

References and Notes

- (1) For recent reviews on hypervalent compounds, see: Akiba, K.-y. In *Chemistry of hypervalent compounds*; Akiba, K.-y., Ed.; Wiley-VCH: New York, 1999; Chapters 1 and 2. Yamamoto, Y.; Akiba, K.-y. *J. Organomet. Chem.* **2000**, *611*, 200.
- (2) Fukin, G. K.; Zakharov, L. N.; Domrachev, G. A.; Fedorov, A. Yu.; Zaboruyaeva, S. N.; Dodonov, V. A. *Izv. Akad. Nauk, Ser. Khim.* **1999**, 1744 [*Russ. Chem. Bull.* **1999**, *48*, 1722 (English translation)].
- (3) Satoh, W.; Masumoto, S.; Shimizu, M.; Yamamoto, Y.; Akiba, K.-y. *Bull. Chem. Soc. Jpn.* **1999**, *72*, 459.
- (4) Carmalt, C. J.; Cowley, A. H.; Culp, R. D.; Jones, R. A.; Kamepalli, S.; Norman, N. C. *Inorg. Chem.* **1997**, *36*, 2770.
- (5) Chuit, C.; Corriu, R. J. P.; Monforte, P.; Reyé, C.; Declercq, J. P.; Dubourg, A. *J. Organomet. Chem.* **1996**, *511*, 171.
- (6) Iwaoka, M.; Tomoda, S. *J. Am. Chem. Soc.* **1996**, *118*, 8077.
- (7) Yamamoto, Y.; Chen, X.; Kojima, S.; Ohdoi, K.; Kitano, M.; Doi, Y.; Akiba, K.-y. *J. Am. Chem. Soc.* **1995**, *117*, 3922.
- (8) Yamamoto, Y.; Nadano, R.; Itagaki, M.; Akiba, K.-y. *J. Am. Chem. Soc.* **1995**, *117*, 8287.
- (9) Iwaoka, M.; Tomoda, S. *J. Org. Chem.* **1995**, *60*, 5299.
- (10) Murafuji, T.; Mutoh, T.; Satoh, T.; Tsunenari, K.; Azuma, N.; Suzuki, H. *Organometallics* **1995**, *14*, 3848.
- (11) Kojima, S.; Doi, Y.; Okuda, M.; Akiba, K.-y. *Organometallics* **1995**, *14*, 1928.
- (12) Nagase, S. In *The chemistry of organic arsenic, antimony and bismuth compounds*; Patai, S., Ed.; Wiley & Sons: New York, 1994; Chapter 1.
- (13) Suzuki, H.; Murafuji, T.; Matano, Y.; Azuma, N. *J. Chem. Soc., Perkin Trans.* **1993**, *1*, 2969.
- (14) David, A.; Cowley, A. H.; Ruiz, J. *Inorg. Chim. Acta* **1992**, 198–200, 271.
- (15) Yamamoto, Y.; Chen, X.; Akiba, K.-y. *J. Am. Chem. Soc.* **1992**, *114*, 7906.
- (16) Stang, P. J. *J. Org. Chem.* **2003**, *68*, 2997.
- (17) Zhdankin, V. V.; Stang, P. J. *Chem. Rev.* **2002**, *102*, 2523.
- (18) Stang, P. J.; Zhdankin, V. V. *Chem. Rev.* **1996**, *96*, 123.
- (19) Seki, H.; Tokunaga, T.; Utsumi, H.; Yamaguchi, K. *Tetrahedron* **2000**, *56*, 2935.
- (20) Tokunaga, T.; Seki, H.; Yasuike, S.; Ikoma, M.; Kurita, J.; Yamaguchi, K. *Tetrahedron Lett.* **2000**, *41*, 1031.
- (21) Tokunaga, T.; Seki, H.; Yasuike, S.; Ikoma, M.; Kurita, J.; Yamaguchi, K. *Tetrahedron* **2000**, *56*, 8833.
- (22) Okajima, S.; Yasuike, S.; Kakusawa, N.; Osada, A.; Yamaguchi, K.; Seki, H.; Kurita, J. *J. Organomet. Chem.* **2002**, *656*, 234.
- (23) Kakusawa, N.; Tobiyasu, Y.; Yasuike, S.; Yamaguchi, K.; Seki, H.; Kurita, J. *Tetrahedron Lett.* **2003**, *44*, 8589.
- (24) For a review on the electrochemistry of stibines: Nielsen, M. F. In *The chemistry of organic arsenic, antimony, and bismuth compounds*; Patai, S., Ed.; Wiley & Sons: New York, 1994; Chapter 11.
- (25) Fuchigami, F.; Miyazaki, M. *Electrochim. Acta* **1997**, *42*, 1979.
- (26) Kadish, K. M.; Autret, M.; Ou, Z.; Akiba, K.-y.; Masumoto, S.; Wada, R.; Yamamoto, Y. *Inorg. Chem.* **1996**, *35*, 5564.
- (27) Le Roux, C.; Ciliberti, L.; Laurent-Robert, H.; Laporterie, A.; Dubac, J. *Synlett* **1998**, 1249.
- (28) Luo, S. G.; Tan, H. M.; Zhang, J. G.; Wu, Y. J.; Pei, F. K.; Meng, X. H. *J. Appl. Polym. Sci.* **1997**, *65*, 1217.
- (29) Boisselier, V. Le; Dunach, E.; Postel, M. *J. Organomet. Chem.* **1994**, *482*, 119.
- (30) Cowley, A. H.; Jones, R. A. *Angew. Chem., Int. Ed. Engl.* **1989**, *28*, 1208.
- (31) Higa, K. T.; George, C. *Organometallics* **1990**, *9*, 275.
- (32) Bard, A. J.; Faulkner, L. R. In *Electrochemical methods*; John Wiley & Sons: New York, 1980; Chapters 6 and 11.
- (33) Delahay, P. In *New instrumental methods in electrochemistry*; Interscience: New York, 1996; Chapter 6.
- (34) Nicholson, R. S.; Shain, I. *Anal. Chem.* **1964**, *36*, 706.
- (35) Hiers, G. S. *Org. Synth., Coll.* **1941**, *1*, 550.
- (36) Akiba, K.-y. *Pure Appl. Chem.* **1996**, *68*, 837.
- (37) Polarographic half-wave potential of **2** was previously reported to be 1.32 V vs SCE in CH_3CN at a Pt electrode: Nikitin, E. V.; Kazakova, A. A.; Parakin, O. V.; Mironov, B. S. Kargin, Yu. M. *Dokl. Akad. Nauk SSSR* **1980**, *251*, 1175.
- (38) Half-wave potential of **5** was previously reported to be 0.975 V vs SCE in CH_3CN at a carbon paste electrode: Matschiner, H.; Krauze, L.; Krech, F. Z. *Anorg. Allg. Chem.* **1970**, *373*, 1.
- (39) Schiavon, G.; Zecchin, S.; Cogoni, G.; Bontempelli, G. *J. Electroanal. Chem.* **1975**, *59*, 195.
- (40) Quite recently, characterization of intramolecular $\text{N} \rightarrow \text{M}$ ($\text{M} = \text{Sb}$ and Bi) bonds in newly synthesized metallatranes were reported: Shutov, P. L.; Karlov, S. S.; Harms, K.; Tyurin, D. A.; Churakov, A. V.; Lorberth, J.; Zaitseva, G. S. *Inorg. Chem.* **2002**, *41*, 6147.
- (41) Gosser, D. K., Jr. *Cyclic Voltammetry – Simulation and Analysis of Reaction Mechanism*; VCH: New York, 1993.
- (42) Appendix B in ref 32.
- (43) For example: Komura, T.; Yamaguchi, T.; Noda, K.; Hayashi, S. *Electrochim. Acta* **2002**, *47*, 3315.
- (44) Savéant, J. M.; Xu, F. *J. Electroanal. Chem.* **1986**, *208*, 197.